

1 Secondary fluorescence in WDS: the role of spectrometer positioning

2 Ben Buse, Jon Wade, Xavier Llovet, Stuart Kearns, and John J Donovan

4 Abstract

5 Secondary fluorescence, typically a minor error in routine electron probe microanalysis (EPMA), may
6 not be negligible when performing high precision trace element analyses in multiphase samples.
7 Other factors, notably wavelength dispersive spectrometer defocusing, may introduce analytical
8 artefacts.

9 To explore these issues, we measured EPMA transects across two material couples chosen for their
10 high fluorescence yield. We measured transects away from the fluorescent phase, and at various
11 orientations with respect to the spectrometer focal line. Compared to calculations using both the
12 Monte Carlo simulation code PENEPM and the semi-analytical model FANAL, both codes estimate
13 the magnitude of SF, but accurate correction requires knowledge of the position of the spectrometer
14 with respect to the couple interface. Positioned over the fluorescent phase or otherwise here
15 results in a factor of 1.2-1.8 of apparent change in SF yield.

16 SF and spectrometer defocusing may introduce systematic errors into trace element analyses, both
17 may be adequately accounted for by modelling. Of the two, however, SF is the dominant error,
18 resulting in 0.1 wt% Zn apparently present in Al at 100 μm away from the Zn boundary in an Al/Zn
19 couple. Of this, around 200 ppm Zn can be attributed to spectrometer defocusing.

20 Introduction

21 Secondary fluorescence (SF), where characteristic x-rays are excited by either continuum- or
22 characteristic x-rays possessing energies above their critical excitation edge, may arise at significant
23 distances from the electron beam point of impact. This can be significant when measuring trace
24 elements in multiphase samples, where the SF contribution arises from adjacent phases containing
25 the element of interest in high concentration (e.g. Adams and Bishop (1986)). Examples include
26 diffusion profile measurements, redox sensors and geo-thermometers (e.g. Ti in quartz). In such
27 cases, it is necessary to subtract the SF contribution to obtain the correct concentration in the phase
28 being analysed; this can be done either by preparing material couples and measuring SF contribution
29 (Adams and Bishop (1986)) or by calculating SF (e.g. Myklebust & Newbury 1995). For high-precision
30 trace element analysis, the positioning of the spectrometer must be considered, to accurately
31 correct for SF (Fournelle et al, 2005; Llovet & Salvat, 2017). This determines the material path – that
32 is, the path through the material by which the fluoresced x-rays travel to the detector - which in turn
33 determines the degree of x-ray absorption (Llovet et al. 2012). Spectrometer placement with respect
34 to the sample also determines the extent to which the source of fluorescent x-rays is in focus with
35 respect to the spectrometer, a factor that is often overlooked. Although the spectrometer is focused
36 on the point of analysis, SF x-rays originate from a range of distances from it (as large as hundreds of
37 microns) and are displaced relative to the focal position.

38 Electron probe microanalysis (EPMA) relies on Rowland circle wavelength dispersive spectrometers
39 (WDS), which utilise a type of Bragg spectrometer where the incident x-rays are reflected into a
40 proportional counter using a crystal. WDS crystals are curved to twice the radius of the Rowland
41 circle upon which the sample, crystal and counter all lie. Typical Rowland circles for commercially
42 available spectrometers range from 100 mm (H-type) and 140 mm for JEOL microprobes, 160 mm
43 for CAMECA microprobes and 210 mm for Oxford Instruments spectrometers. On a JEOL microprobe

44 the suffix H e.g. PETH denotes a PET crystal on a H-type spectrometer, whilst the suffix L e.g. PETL
45 denotes a large PET crystal on a regular 140 mm Rowland circle.

46 Two variants of reflecting crystals are employed; a Johann and a Johannson type crystal, the latter in
47 addition to being curved is ground to the radius of the Rowland circle. In both cases the curvature of
48 the reflecting crystals maximises the solid angle of the incident x-rays. SF arises when x-rays are
49 excited in a neighbouring phase by x-rays possessing energies above the critical excitation energy of
50 the fluoresced x-rays. These SF x-rays may therefore be excited a significant distance from the point
51 of analysis and, given the spectrometers finite focal area, may be collected in addition to those
52 originating from the analytical point.

53 Spectrometer defocusing is most readily observed when a beam scan x-ray map (using a rastered
54 beam) is acquired over a large area; the spectrometer is in focus along a line perpendicular to the
55 plane of the Rowland circle (Figure 1a), but counts diminish away from the centre of the focal line
56 (e.g. Newbury et al. 1988). This defocusing arises when the x-ray source, crystal and detector no
57 longer lie on the Rowland circle and the spectrometer deviates from the geometry required to
58 satisfy the Bragg equation. As the source becomes displaced, spectrometer defocusing is at a
59 maximum in the plane of the Rowland circle (displacement in x on Fig 1a) and diminishes to zero
60 perpendicular to the plane of the Rowland circle (displacement in y on fig 1a). The amount of
61 defocusing resulting from the displacement of the source in x, expressed in terms of the change in
62 $\sin(\theta)$ angle reflected, is given by the equation:

$$63 \sin(\Delta\theta) = \Delta x \sin(\psi) / 2R \sin \theta \quad (1)$$

64
65 where $2R \sin \theta$ is the distance between the x-ray source and reflecting crystal, Δx is the amount of
66 lateral source displacement, ψ is the take-off angle (40°) and R is the radius of the Rowland
67 circle (Marinenko et al. 1988). Hence, spectrometer defocusing can be reduced by increasing the
68 distance between the x-ray source and reflecting crystal; for example, for elements which may be
69 analysed on several crystals, using the reflecting crystal with the smaller d-spacing, Ti on LIF for 140
70 mm Rowland circle $2R \sin \theta = 191$ mm compared to 87.9mm on PET. The impact of defocusing on x-
71 ray intensities will vary with spectral resolution. Although only vertical spectrometers are considered
72 in this study, inclined spectrometers exhibit poorer lateral resolution due to the focal plane being
73 inclined relative to the vertical. Therefore, any influence arising from spectrometer defocusing will
74 be greater for spectrometers orientated away from the vertical.

75 The influence of spectrometer defocusing on measured SF contributions was first suggested by
76 Adams and Bishop (1986) to explain discrepancies in measured and calculated SF contributions, and
77 subsequent work (e.g. Dalton and Lane 1996, Llovet & Galan 2003) attempted to measure SF along
78 the "focus line of the spectrometer" (Dalton & Lane 1996). If spectrometer defocusing is not
79 considered, any SF correction made by assuming the shortest linear distance from point of analysis
80 to the fluorescent phases may result in an over-correction, and hence the concentration in the
81 sample will be under-estimated.

82 To assess the importance of spectrometer orientation on trace element analyses in multiphase
83 samples, we measure the SF contribution at various orientations with respect to the detector focal
84 line and with different material paths to the detector. The aim is to evaluate the various errors
85 associated with spectrometer positioning. We show that a low magnification beam scan map may be
86 used to obtain a good agreement between measured and modelled SF contributions. Moderate
87 corrections are required when the spectrometer is defocussed – that is, when the fluorescent phase
88 does not lie along the spectrometer's line of focus. This approach of correction for both SF as a
89 function of spectrometer position with respect to the fluorescing phase boundary, and the potential

90 for spectrometer defocusing, allows for a correct subtraction of SF and hence accurate trace
91 element analyses in multiphase samples.

92 [Materials and methods](#)

93 To quantify the effect of spectrometer defocusing, an aluminium and zinc metal material couple was
94 made using spectroscopically pure metals. These were chosen for the significant Zn SF that arises
95 when measuring Al metal at large distances from the interface, especially when using high
96 accelerating voltages. The two metals were pressed together and set in epoxy resin resulting in a
97 good contact such that there was no physical gap apparent along the join. A second couple made of
98 molybdenum and titanium was prepared in a similar fashion. The SF contribution of Zn K α arising
99 from SF was measured along transects through the Al, with the spectrometers aligned on the Al side
100 of the couple (here referred to as the Al-path). All the transects were measured perpendicular to the
101 material interface with Zn. The orientation of the sample with respect to the focal line of the
102 detector, given by angle α , was varied (see figure 1b), with transects measured at $\alpha = 0^\circ$ - i.e. with
103 the material boundary lying perpendicular to the focal plane - and at α angles in the range $10-90^\circ$
104 (see Figure 1). In the case of the transect measured at $\alpha = 0^\circ$, the x-rays pass along the interface to
105 the detector through both components of the couple, requiring further considerations when
106 modelling. Transects made at α angles in the range $10-90^\circ$ avoid this complication since the
107 resultant x-rays pass solely through one half of the material couple. In addition, secondary
108 fluoresced Zn x-rays were also measured with the spectrometers aligned on the Zn side of the
109 couple (the Zn-path). By measuring the effect of the spectrometer placement with respect to the
110 material boundary, we can assess the effect that the material path – here either Al or Zn – has on
111 the measured SF yield. To remove any possibility of extraneous fluoresced x-rays arising from the
112 sample holder, we used an aluminium sample holder - measurement of a zinc-free aluminium
113 standard confirmed the absence of other Zn contributions. Measurements were made on a JEOL
114 8530F electron microprobe, at the University of Bristol, using a LIFH crystal. Analytical conditions
115 were chosen to maximise the SF signal, with an accelerating voltage of 30 kV, a beam current of 500
116 nA, and a spot size of 1 μm . Count times were 60 seconds on peak and 60 seconds on background.
117 Zn was measured whilst the Al content was specified.

118 To explore the effects of SF arising from softer x-rays excited when analysing a denser material, we
119 used a similar approach with a Ti-Mo couple, with the SF contribution of Ti K α measured along
120 several transects through the Mo. In this example, the transects were oriented at $\alpha = 11.5^\circ$ and $\alpha =$
121 101.5° . The specific orientation of these transects was motivated by the azimuthal position of the
122 spectrometer around the electron optics system (-11.5° with respect to the horizontal X-axis). These
123 orientations mean the SF x-rays were only absorbed in the Ti side of the couple, which allows direct
124 comparison with the geometries assumed by the FANAL calculations (see below). The
125 measurements were made on a JEOL 8230 electron microprobe using a PETL crystal, at the
126 University of Barcelona. Analytical conditions were an accelerating voltage of 25 kV, a beam current
127 of 500 nA, and a nominal spot size of 1 μm . Again, count times were 60 seconds on peak and 60
128 seconds on background.

129 Since the SF arises from a neighbouring phase, there is no appropriate matrix correction. For clarity,
130 we therefore report k-ratios as apparent wt. % or apparent ppm.

131 [Modelling secondary fluorescence](#)

132 We calculated the SF contribution using the Monte Carlo simulation programme PENEPMA (Llovet
133 and Salvat, 2017). Two detectors were simulated, both of 180° azimuthal aperture collecting x-rays
134 between $35-45^\circ$ take-off angle, positioned either side of the material couple boundary. The large

135 semi-circular detectors both reduce simulation time and increase precision. This geometry allows
136 direct comparison with FANAL calculations, which presume the detector is positioned only over the
137 side of the fluorescing material. The simulations achieved a 1% relative error (at 3 sigma level) on
138 both the standard intensity and the unknown intensity at short distances from the interface (≤ 75
139 μm), rising to 4% at 450 μm . For the special case of a transect oriented parallel to the focal line of
140 the detector, where x-rays pass through two materials on route to the detector, the effect of the
141 azimuthal width ($\Delta\phi$) of the detector aperture on modelled results was investigated. Simulations
142 were made at 100 μm with a detector aligned to the material interface and the azimuthal width was
143 varied.

144 FANAL provides an easy and fast calculation of SF (Llovet et al. 2012; Donovan et al 2012) but, unlike
145 PENEPMA, implements only a semi-analytical model for the calculation of SF near a planar,
146 perpendicular material boundary. FANAL obtains the intensities of primary photons for both
147 materials used in the couple and the standard, using a version of PENEPMA optimized for this task
148 (see Llovet et al 2012). Importantly, the approach taken in the FANAL code makes two assumptions
149 – firstly that the detector is located only over the fluorescing phase, and secondly that the
150 emission of bremsstrahlung photons is isotropic. The first assumption means that only x-ray
151 absorption through the fluorescent phase needs to be considered, whilst the second greatly
152 simplifies the analytical model upon which FANAL is based.

153 To correct for secondary fluorescence the modelled SF k-ratios are subtracted from the experimental
154 k-ratios, which should be first corrected for spectrometer defocusing.

155 Correction for spectrometer defocusing

156 To adequately account for the influence of SF on trace element analysis, it may be necessary to
157 calibrate the analytical spectrometer's rate of defocusing with respect to distance from the focal
158 line. This was achieved by acquiring x-ray maps, with the beam rastered over a large area (fig 2), on
159 Zn and Ti metal standards. This allows the reduction in x-ray intensity as a result of spectrometer
160 defocusing to be calculated as follows. Firstly, x-ray counts were extracted from a line (X-Y; Figure 2
161 a & b) possessing the same orientation as the transect. For example, Figure 2 shows the
162 measurements of the material couple where the Zn interface (source of Zn X-rays) was to the top left
163 with respect to the electron beam point of impact (position of spectrometer focus). Secondly, the
164 ratio of maximum intensity to measured intensity was calculated and described using a polynomial
165 function (the polynomial required varied between 2nd to 6th order to achieve a data fit of
166 approximately $\pm 2\%$ relative). To correct for defocusing, the measured data was then multiplied by
167 the polynomial function, with x being the distance to the interface. Note that we implicitly assume
168 that SF is emitted from a single point located on the interface of the two materials.

169 Results

170 Zn-Al couple

171 Transects where x-rays pass through a single material to detector

172 Figure 3 shows the results for both PENEPMA and FANAL simulations for a transect in Al away from
173 the Zn interface. Zn K α k-ratios are greater where the material path to the detector is aluminium (Al-
174 path) by a factor of 1.2 increasing to 1.8 with distance. The difference between the paths is due to
175 the lower x-ray absorption of Zn in Al (Llovet et al. 2012). In general, the two codes show a good
176 agreement although the assumptions made in the FANAL model mean that it can only be compared
177 to PENEPMA where Zn is the material path to the detector (Zn-path) – i.e. where the simulated
178 PENEPMA detector is located over the Zn (fluorescent) component of the couple. The slight
179 deviations between the two models likely relate to the treatment of the bremsstrahlung emission

180 which FANAL assumes to be emitted isotropically, whilst PENEPMA uses an intrinsic theoretical
181 angular distribution (Acosta et al. 2002, Llovet et al. 2011). Here the simplification used by the
182 FANAL model becomes important since all the SF results from bremsstrahlung emission rather than
183 primary x-ray emission.

184 Experimental results for the Zn-Al couple are shown in Figure 4. The measured zinc k-ratio decreases
185 with distance from the interface as the influence of SF decreases. Fig 4a shows the situation
186 assumed by FANAL (see Figure 3), where the spectrometer is located over the fluorescing phase
187 (here the Zn-path), while (4b) shows the results for the Al-path. At distances $< 100\mu\text{m}$, assuming the
188 correct sample geometry is used, that is, the correct material path to the detector is simulated, the
189 measurements show a reasonable approximation to the modelled data. The measured intensities for
190 the Al-path are, however, higher than the Zn-path due to lower x-ray absorption. At distances > 100
191 μm the measured intensities are lower than predicted by PENEPMA which is consistent with
192 spectrometer defocusing.

193 To show the magnitude of defocusing effects, the residual concentration, that is, the amount of
194 measured Zn that remains apparent in the sample after SF contributions are accounted for, is shown
195 in figure 5. This shows the residual when SF alone and SF plus a defocusing correction is subtracted
196 from the measured concentrations. All the Zn is derived from SF and therefore the residual should
197 be zero. Simply correcting for SF results in a small negative residual (hundreds of ppm), which is a
198 small percentage of SF contributions (thousands of ppm) at short distances, but this becomes
199 increasingly significant at longer distances as the SF contributions are reduced. Adjusting the
200 measured data for defocusing effects decreases the residual over distances 50-200 μm over which
201 defocusing is significant. At distances $> 200\mu\text{m}$ correcting for defocusing is problematic, and results
202 in a significant over correction. Additionally, at these distances defocusing is severe, but the
203 measured SF contribution does not decrease as one may expected. The reasons are unclear and may
204 reflect fluorescence of the Zn material from chamber scattered x-rays.

205 **Transects where x-rays pass through two materials to detector**

206 Here the instrument detector is aligned along the material interface. Simulations using a similar
207 geometry show the modelled results are strongly dependent on the detector aperture width (figure
208 6), and a realistic aperture width is required. On a JEOL EPMA, the distance of the analytical source
209 from the reflecting crystal, in this case a LIFH crystal reflecting Zn $K\alpha$ radiation, is 71 mm. The
210 reflecting crystal position corresponds to the detector in the simulation, and a typical crystal is
211 approximately 1.7 cm wide resulting in a 10° azimuthal aperture being a reasonable approximation
212 for the purposes of the simulation. Due to the small solid angle of the simulated detector,
213 simulations were only made for a single point along the transect in Al, 100 μm from the interface.
214 Using this simulation, the more computationally efficient 180° azimuthal aperture may be used to
215 correct the Zn-path modelled results, by applying a scaling factor (the difference in k-ratio between
216 the Al-Zn path with a 10° azimuthal aperture and the Zn path with a 180° azimuthal aperture, at 100
217 μm).

218 Figure 7 compares the experimental and modelled results. The experimental results show a
219 reasonable agreement with the simulation data for a 10° azimuthal aperture, which approximates
220 the effective width of a real detector. If this is neglected a substantial error results if the Al path to
221 detector is used.

222 Ti-Mo couple

223 In the case of the measure Ti K α k-ratio, there is a satisfactory agreement between the predictions of
224 FANAL and PENEPM (Figure 8). In a high-Z element, such as Mo, electron trajectories are more
225 rapidly randomized by elastic scattering than in a low-Z material, such as Al. The angular distribution
226 of continuum photons is therefore less sensitive to their intrinsic angular distribution. The higher
227 density material present in the couple – in this case Mo - significantly increases the absorption of
228 bremsstrahlung x-rays, resulting in greater attenuation and hence a lower SF contribution with
229 distance increases from the boundary. This results in lessening of the influence of SF with distance –
230 for the Al-Zn couple, Zn SF was measured at 200 ppm at a distance of 300 μ m, whilst Ti reaches 200
231 ppm at only 40 μ m from the boundary. This rapid attenuation of fluoresced x-rays results in minimal
232 defocusing observed at $\alpha = 101.5^\circ$ and within the analytical error. The small magnitude of the
233 defocusing effect compared to the SF contribution, over these distances, is clearly seen in the
234 comparison of the two curves in (fig 8b). The position of the detector with respect to the interface
235 results a change in concentration of a factor of 1.25. This is a larger error than that generated by
236 spectrometer defocusing close to the interface, but the error associated with defocusing increases to
237 comparable magnitude at the long distances.

238 Again, the correction for spectrometer defocusing proposed here assumes that SF is emitted from a
239 single point, located precisely on the interface. PENEPM simulations show that Ti K α x-rays emitted
240 from a Ti-Mo couple do not arise from a point source; when the beam impacts at 25 μ m from the
241 boundary, the maximum region over which the Ti K α x-rays are actually generated extends up to
242 ~ 150 μ m either way along the boundary direction and ~ 100 μ m into the Ti (Figure 9). However,
243 the maximum intensity is localized close to the boundary, with 75% of the excited x-rays generated
244 within 40 μ m either way along the boundary and 40 μ m into the Ti, and rapidly decreases in both
245 directions. Given the complexities and material specific nature of the excitation volume, and the
246 limited volume over which the majority of SF x-rays are generated, a point source was assumed to
247 be a valid assumption for the purpose of correcting spectrometer defocusing.

248 To calculate the error associated with using this assumption, the results were compared to a more
249 accurate 2D defocusing correction using simulated x-ray emission maps (see Fig 9) as follows: for
250 selected distances to the boundary (10, 25, 50 and 100 μ m), the simulated x-ray emission maps were
251 multiplied pixel by pixel by the defocusing map and the resulting maps were integrated so as to yield
252 the corrected x-ray intensities at the specific distance.

253 These intensities were then compared with those obtained by using one single pixel for the
254 correction (the first pixel situated along the transect within the fluorescing phase). The
255 difference between assuming an x-ray emission region and an x-ray emission point for the
256 defocusing correction was found to be less than 5%. Nevertheless, the difference between the
257 experimental data and the calculated data (corrected for defocusing effects assuming a point x-
258 ray source) appears to be larger than 5%. The reason for this disagreement is not fully understood,
259 and it would obviously be interesting to make similar measurements and calculations in other
260 systems.

261 Discussion

262 The ability to rapidly estimate the SF contribution arising from neighbouring phases and correct for
263 their influence on minor and trace element analyses, has proven valuable, especially where high
264 spatial resolution analysis (Wade and Wood, 2012) or element diffusion profiles are desired. On the
265 other hand, the orientation of the spectrometer with respect to neighbouring, fluorescent phases
266 has been largely overlooked, even though its effect may not be negligible if high accuracy analyses
267 are required. Although simulation codes are capable of adequately correcting for SF in real analyses,

268 they do require knowledge of both sample and spectrometer geometries such that they do not over-
269 or under compensate. The correction process, detailed above, allows the SF contributions for
270 varying spectrometer orientations to be calculated, which may then be subtracted from
271 measurements to give the primary x-ray intensity. This requires knowledge of the transect
272 orientation with respect to the spectrometer's focal line and a beam scan map of the spectrometer
273 from which the intensity loss with source displacement can be calculated. In the case that several
274 spectrometers are used to improve counting statistics (see e.g. Wark and Watson, 2006), the
275 proposed correction should be applied to the x-ray intensities measured by each spectrometer,
276 before obtaining the sum of all intensities. To minimise instrument time, a beam scan map could be
277 calculated from a WD peak scan using the method of Myklebust et al. (1986), since the effect of
278 scanning the beam (deflecting the source) in the plane of the Rowland circle is equivalent to shifting
279 the crystal angle (Myklebust et al. 1986, Swyt & Fiori 1986).

280 In most scenarios, spectrometer defocusing represents, at worst, only a minor correction to trace
281 element analyses compared to the influence of SF, and is most likely lost within the analytical
282 uncertainty. For instance, in the example of the Al-Zn couple here, not compensating for defocusing
283 results in a relative error of 6% or 140 ppm Zn, compared to that generated by SF of 2160 ppm at 50
284 μm from the interface. The errors, however, rapidly increase at long distances where defocusing is
285 20% and 60% of that generated by SF at 100 μm and 200 μm respectively. The approach used here
286 with a simple material couple, with a planar, vertical boundary, is well suited to modelling and
287 correction using FANAL, provided the fluorescing material forms the path to the detector. Many real-
288 world samples however, require more robust simulation using PENEPMA which allows for greater
289 flexibility in sample geometries, although it should be noted that for large distances from the
290 boundary the effect of geometry will be small. The results for a planar couple however, provide
291 insight on the circumstances for which a correction for defocusing would be most beneficial and
292 occurs at relatively long distances ($> 50\text{-}100 \mu\text{m}$) to the material boundary. At very long distances (\geq
293 $300 \mu\text{m}$), corrections arising from spectrometer defocusing may be very large (700%-1400%).
294 Importantly, the results suggest a tendency to overcorrect at these long boundary distances. Under
295 these circumstances counting errors are magnified and measurement is unadvisable, with
296 reorientation of the sample to avoid defocusing being preferable whenever possible.

297 The need to account for spectrometer defocusing therefore only arises where the effect on SF
298 contribution arising from spectrometer orientation constitutes a significant part of the error budget.
299 This is most problematic where the material analysed is low density, has minimal attenuation of the
300 fluorescing x-ray, and the resultant SF x-ray has a relatively high fluorescence yield, such as in the Al-
301 Zn couple used here.

302 The placement of the detector with respect to the fluoresced side of the interface results in a
303 significant error - in the case of the Al-Zn couple, the relative difference between a spectrometer
304 placed on one side or other of the boundary results in a factor of 1.2-1.8 change in SF yield.
305 Additionally, the error increases with distance from the interface, but its magnitude and variation
306 with distance depends on the difference in absorption between the two materials, and is greatest
307 where there is a significant difference in density or mass attenuation coefficient. In the case of Ti-Mo
308 the spectrometer placement resulted in an error of 1.25 which varied little with distance. Measuring
309 Ti in quartz, an often used geo-thermometer, provides a good example of where accounting for
310 spectrometer orientation is important. SF of Ti in quartz is observed at long distances away from
311 adjacent materials (e.g. rutile); Wark and Watson (2006) measured 100 ppm in quartz at 100 μm
312 away from rutile (using a quartz-rutile material couple). At this distance, for maximum spectrometer
313 defocusing, measured SF contributions would be reduced by about 30 % using a PET crystal. In

314 addition to spectrometer orientation, switching from PET to LIF would reduce defocusing by
315 increasing the source to crystal distance at which Ti K α is measured but at the expense of x-ray
316 intensity.

317 Spectrometer orientation is less important for SF of Ca in olivine. Dalton and Lane (1996) showed
318 that Ca is fluoresced at significant concentrations up to ca. 40-80 μm from interfaces with phases
319 containing Ca. This equates to intensity reductions for maximum spectrometer defocusing of 15-
320 25%. The requirement for correcting for spectrometer orientation will therefore depend on the
321 degree of defocusing (the orientation of the interface with respect to the detector) and the
322 analytical error (see Dalton & Lane 1996, Llovet et al. 2012).

323

324 Conclusions

325 The SF contribution may result in substantial errors when measuring trace elements at high precision
326 in multiphase samples. The ability to accurately calculate the SF contribution to allow for its
327 subtraction and give actual elemental concentrations depends significantly on spectrometer
328 orientation. Spectrometer orientation is important in determining the material through which x-rays
329 pass through to the detector, and this results in a substantial variation in the SF contribution, both
330 observed and simulated. Spectrometer orientation may result in a reduction of the measured SF
331 where the source of SF x-rays is defocused with respect to the spectrometer. This effect is small
332 compared to the SF contribution, although at long distances its contribution can change the
333 apparent SF by tens of percent relative. Defocusing effects on SF are at a maximum when interfaces
334 are perpendicular to the plane of the Rowland circle (parallel to the spectrometer line of focus).
335 Ignoring these effects leads to a small but systematic error in our ability to correct SF contribution
336 and subtract it from measurements to give primary x-ray intensities.

337 At short distances, errors from spectrometer defocusing are not significant given the other errors
338 involved in calculating the SF contribution. However, where the reduction in intensity from
339 spectrometer defocusing exceeds errors associated with the SF calculation, it should be considered.

340 In the example of Ti-Mo, SF decreases rapidly from the interface and error arising from defocusing is
341 within analytical error. In contrast, the example of Zn fluoresced from an Al-Zn couple, SF extends a
342 significant distance from the interface and defocusing results in a significant error. The error is in
343 excess of 20% of the SF contribution at distances $> 100\mu\text{m}$, and exceeds the analytical error of 3%
344 relative (at 3 sigma level) at $100\mu\text{m}$. Defocusing errors may be addressed by either:

- 345 (a) reducing defocusing by selecting a reflecting crystal with a smaller d-spacing. This is however
346 accompanied by a loss of x-ray intensity.
- 347 (b) correcting the measured intensities for spectrometer defocusing prior to correcting for SF.

348

349 Transects at small angles to the focal line of the detector are obviously preferable. However, in the
350 case of transects made parallel to the focal line, with x-rays passing along the interface to the
351 detector, the aperture of the instrument detector must also be considered and used to scale the
352 simulated results.

353 The results presented here suggest spectrometer defocusing has a large effect on measured SF
354 intensities at distances $> 50\text{-}100\ \mu\text{m}$ from the source of x-rays. This is, however, dependent both on
355 the width of the x-ray peak and spectrometer resolution.

356 The examples given demonstrate the importance of correcting SF by simulating realistic geometries
357 which correspond to the sample geometry and the instrument configuration; critically the position
358 of the detector with respect to the material interface must be replicated. The current FANAL code
359 works well when the instrument detector is on the fluorescent side of the boundary and x-rays pass
360 through a single material to the detector, giving fast accurate results for this situation. However,
361 care must be taken when relating this to real-world analyses of SF arising from a planar, or non-
362 symmetrical, boundary. In these cases, incorrect assumptions regarding the geometry of the
363 boundary and spectrometer when using simulations to remove these effects, may result in relative
364 errors in excess of 100%. The more detailed approach allowed by PENEPMA allows accurate
365 calculation of SF for all geometries but does require the appropriate geometry to be configured in
366 the input files.

367

368

369 Acknowledgements

370 We would like to thank Charles Clapham (University of Bristol) for his assistance in making the Al-Zn
371 material couple and Erkki Heikinheimo (Aalto University) for preparing the Ti-Mo couple. We would
372 like to thank the reviewers for their detailed comments.

373

374 References

375

376 Acosta, E., Llovet, X., & Salvat, F. (2002). Monte Carlo simulation of bremsstrahlung emission by
377 electrons. *Appl Phys Lett* **80**, 3228–3330.

378 Adams, G. E. & Bishop, F. C. (1986). The olivine-clinopyroxene geobarometer: experimental results in
379 the CaO-FeO-MgO-SiO₂ system. *Contrib Mineral Petrol* **94**, 230-237

380 Bragg, W.H. & Bragg, W.L. (1913). The reflection of X-rays by crystals. *Proc R Soc Lond A Math Phys*
381 *Sci* **88**, 428-438

382 Dalton, J.A. & Lane, S.J. (1996). Electron microprobe analysis of Ca in olivine close to grain
383 boundaries: The problem of secondary X-ray fluorescence. *Am Mineral* **81**, 194-201

384 Donovan, J., Llovet, X., & Salvat, F. (2012). High Speed Matrix and secondary fluorescence effects
385 from fundamental parameter Monte Carlo calculations. *Microsc Microanal* **18**, 1742-1743

386 Fournelle, J., Kim, S., Perepezko, J.H. (2005) Monte Carlo simulation of Nb Ka secondary fluorescence
387 in EPMA: comparison of PENELOPE simulation with experimental results, *Surf. Interface Anal* **37**,
388 1012-1016

389 Kluckner, M., Brandl, O., Weinbruch, S., Stadermann, F.J., Ortner, H.M. (1997) A Method to Correct
390 Defocused Element Distribution Maps in Electron Probe Microanalysis, *Mikrochim. Acta* **125**, 229-
391 234

392 Llovet, X. & Galan, G. (2003). Correction of secondary X-ray fluorescence near grain boundaries in
393 electron microprobe analysis: Application to thermobarometry of spinel lherzolites. *Am Mineral* **88**
394 121-130

395 Llovet, X., Pinard, P.T., Donovan, J.J. & Salvat, F. (2012). Secondary fluorescence in electron probe
396 microanalysis of material couples. *J Phys D: Appl Phys* **45** 225301 (12pp)

397 Llovet, X., & Salvat, F. (2017). PENEPA: A Monte Carlo Program for the Simulation of X-Ray
398 Emission in Electron Probe Microanalysis. *Microsc. Microanal.* **23**, 634–646, 2017

399 Marinenko, R.B., Myklebust, R.L., Bright, D.S. & Newbury, D.E. (1989). Defocus modelling correction
400 for wavelength dispersive digital compositional mapping with the electron microprobe. *J Microsc*
401 **155**, 183-198

402 Myklebust, R.L., Newbury, D.E., Marinenko, R.B. & Bright, D.S. (1986). Defocus modeling for
403 compositional mapping with wavelength dispersive x-ray spectrometry. In *Microbeam Analysis-*
404 *1986*, Romig Jr., A.D. & Chambers, W.F. (Eds.) pp. 495-497. San Francisco : San Francisco Press.

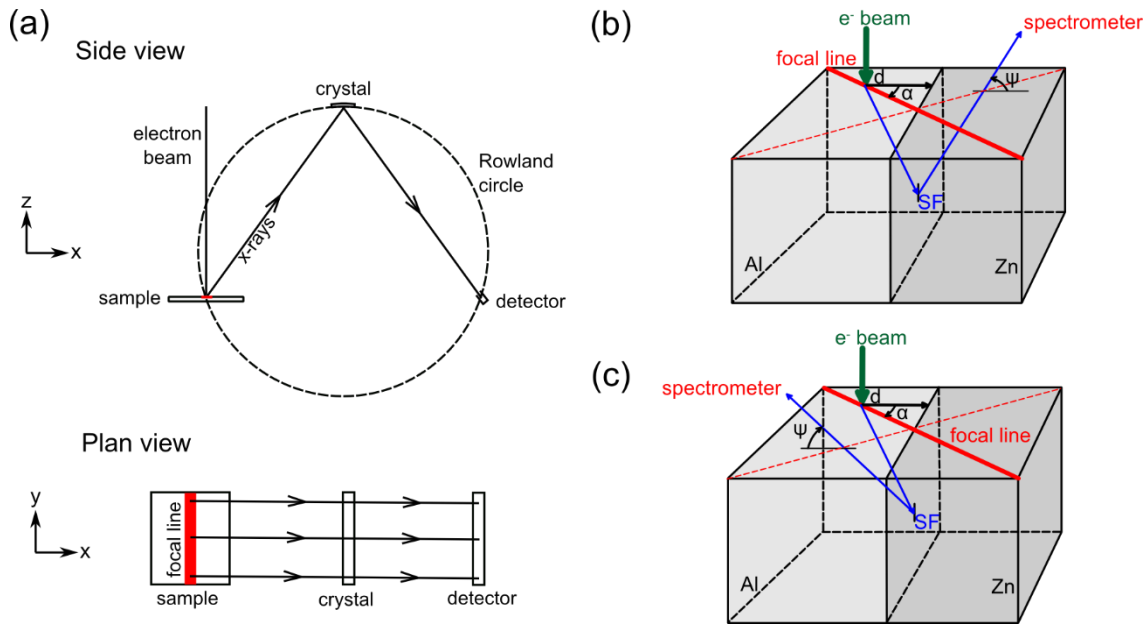
405 Myklebust, R.L. & Newbury, D.E. (1995). Monte carlo modelling of secondary x-ray fluorescence
406 across phase boundaries in electron probe microanalysis. *Scanning* **17**, 235-242

407 Newbury, D.E., Marinenko, R.B., Bright, D.S. & Myklebust, R.L. (1988). Computer-aided imaging:
408 Quantitative compositional mapping with the electron probe microanalyzer. *Scanning* **10** 213-225

409 Swyt, C.R. & Fiori, C.E. (1986). Large-field x-ray compositional mapping with multiple dynamically
410 focussed wavelength-dispersive spectrometers. In *Microbeam Analysis-1986*, Romig Jr., A.D. &
411 Chambers, W.F. (Eds.) pp 482-484. San Francisco: San Francisco Press

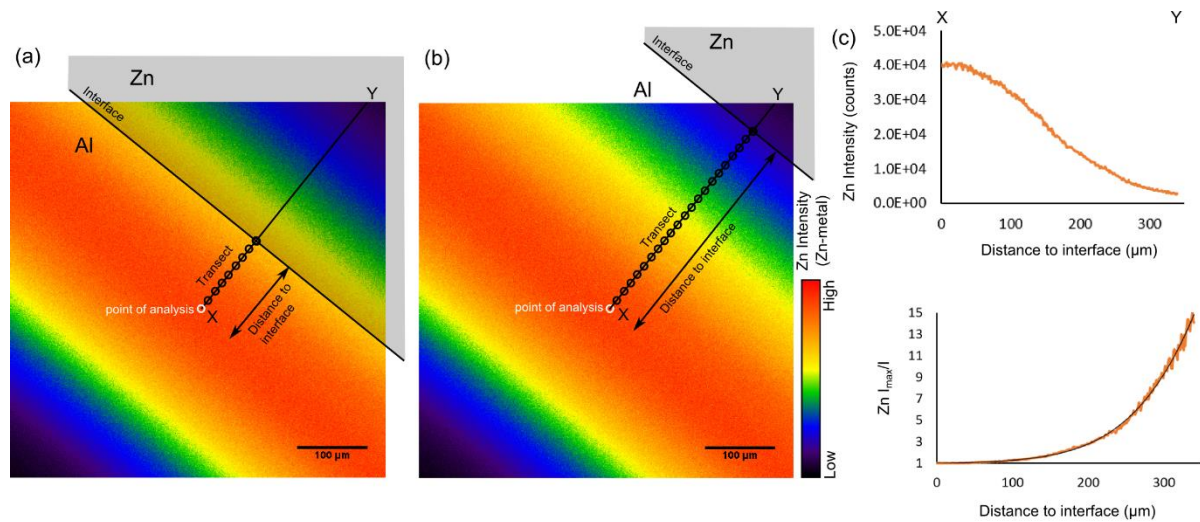
412 Wade, J. & Wood, B. J. (2012). Metal-silicate partitioning experiments in the diamond anvil cell: A
413 comment on potential analytical errors. *Phys Earth Planet Inter* **192-193**, 54-58

414 Wark, D.A. & Watson, E.B. (2006). The TitaniQ: A Titanium-in-quartz geothermometer.
415 *Contrib Mineral Petrol* **152**, 743–754
416



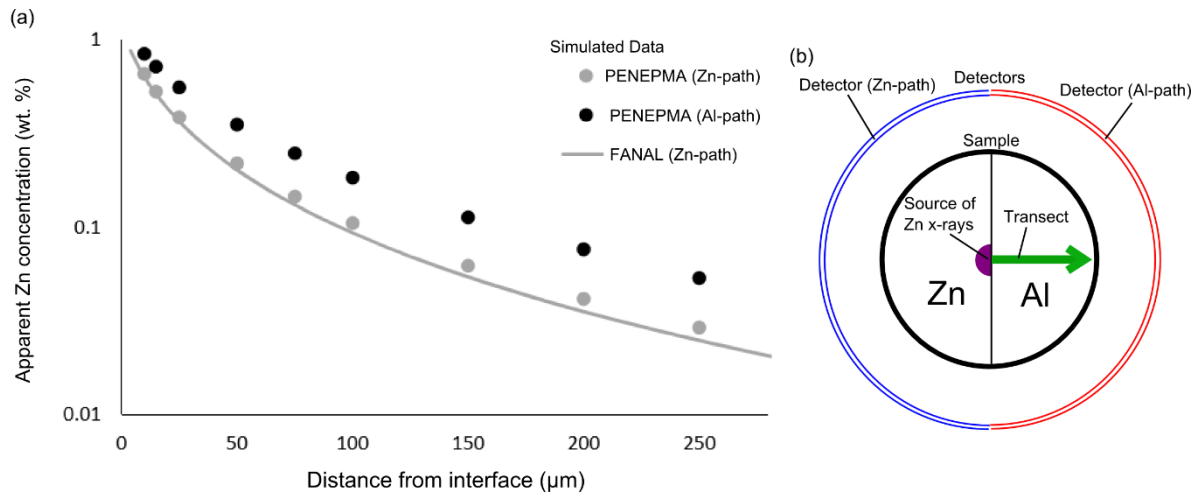
417
418
419
420
421
422
423
424

Figure 1. (a) Schematics showing the orientation of the spectrometer focal line with respect to the Rowland circle. (b & c) Schematic diagrams showing the emission of SF from an Al-Zn couple when the electron beam impinges on the Al phase, at a distance d from the interface. The measuring spectrometer is located on the Zn phase for (b) and on the Al phase for (c). The SF transect is measured along a line perpendicular to the interface and oriented at an angle α with respect to the focal line of the spectrometer. α is changed by rotating the sample. ψ is the take-off angle.

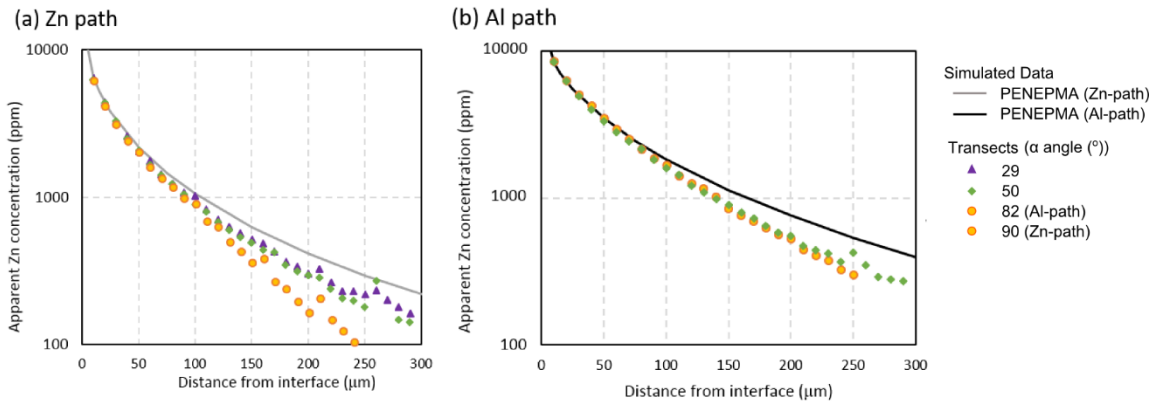


425
426
427
428
429
430
431
432
433
434

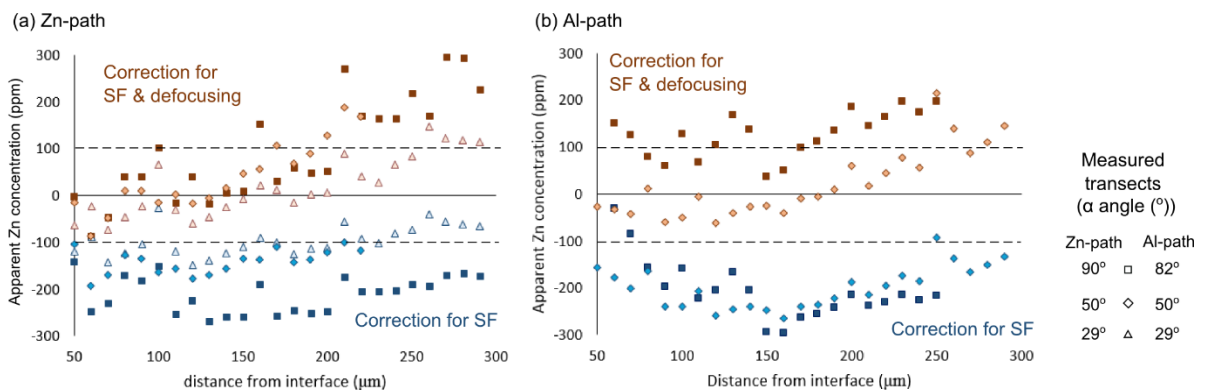
Figure 2. To correct transects for defocusing, a beam scan map is used - this records spectrometer defocusing as the source is displaced away from the focal line. (a, b) Experimental configuration of the transect orientated at 90° to focal line, overlain on the beam scan map acquired on a Zn metal standard. This approach allows the extraction of a line profile from the beam map shown in fig 4c. As the distance to the interface is increased, the spectrometer defocusing becomes pronounced - this is illustrated by the drop in Zn intensity from (4a) to (4b). (c) Extracted intensity for the line profile shown in fig 4a (4c top). The ratio of maximum x-ray intensity to intensity along the line profile, I_{max}/I (4c lower), is used to correct the transect measurements by fitting a polynomial function.



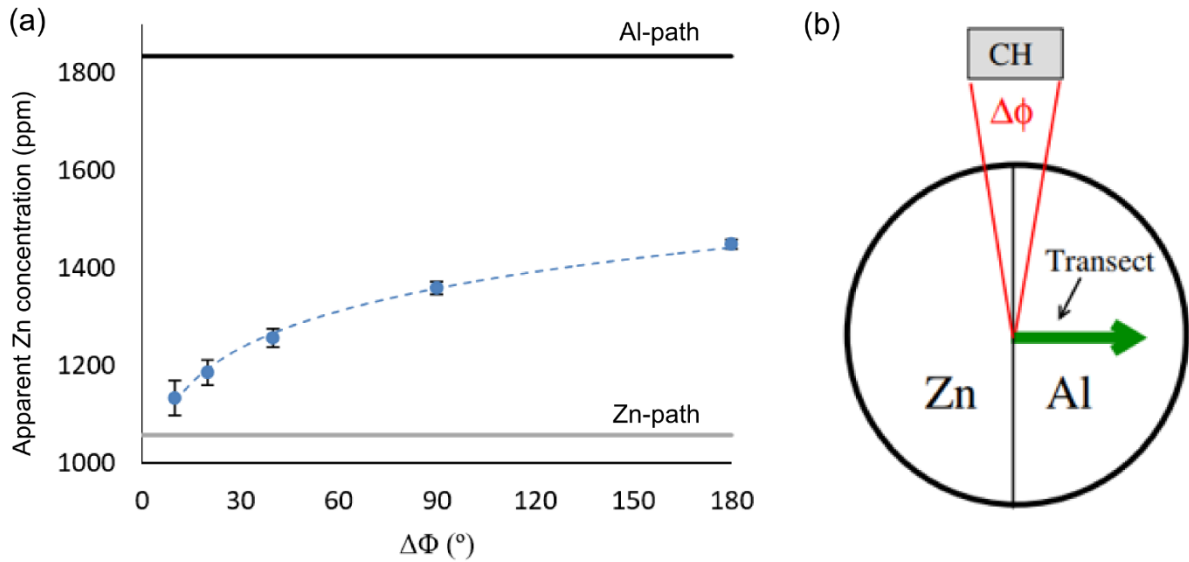
435 Figure 3a. Calculated contributions from Zn secondary fluorescence arising from analysis of Al in a Zn-Al
 436 couple. Depending on the position of the detector, the fluorescent Zn x-rays pass through either Zn or Al
 437 (2b). Calculations are made using both PENEPMA and FANAL; FANAL assumes that x-rays pass through
 438 the material being fluoresced (here Zn).
 439
 440



441 Figure 4. Measured SF contributions of Zn K α in Al for different sample orientations and paths to the
 442 detector: (a) Zn path to detector, (b) Al path to detector. To illustrate the error when using the wrong
 443 detector position, the concentration calculated from a detector on the opposite side of the material
 444 interface is shown. Symbol size approximates analytical errors (3σ).
 445
 446

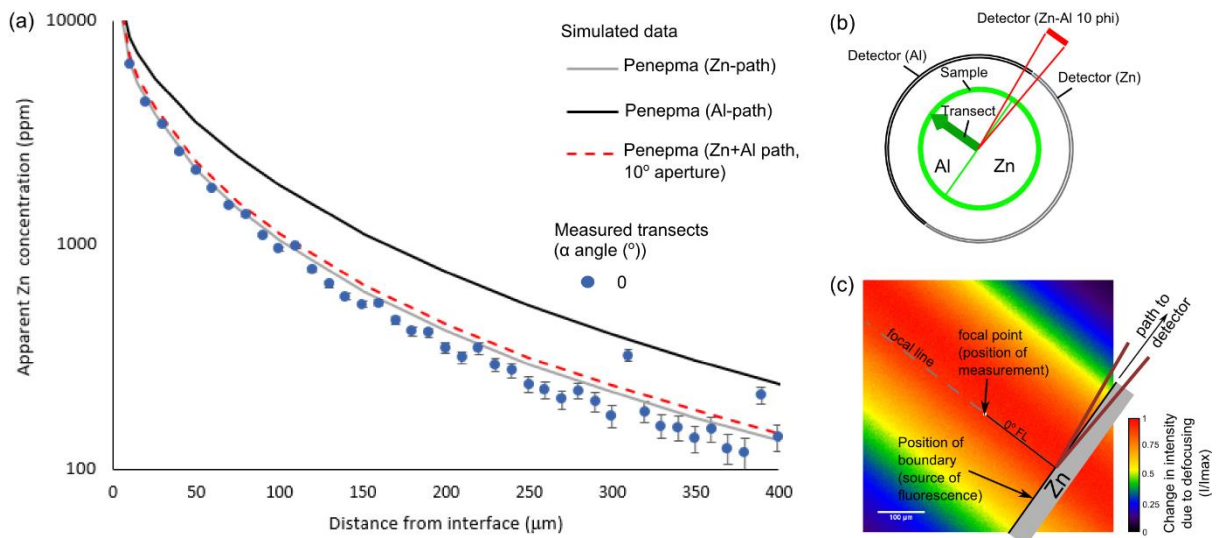


447 Figure 5. Correcting the measured transects which suffer defocusing for SF (blue colours) and SF plus
 448 defocusing (red-orange colours). All the Zn K α originates from SF and therefore the corrected data
 449 should equal zero. To illustrate the improvement made by correcting the data for defocusing, a zone +/-
 450 100 ppm is marked on the graphs by dashed lines.
 451
 452
 453



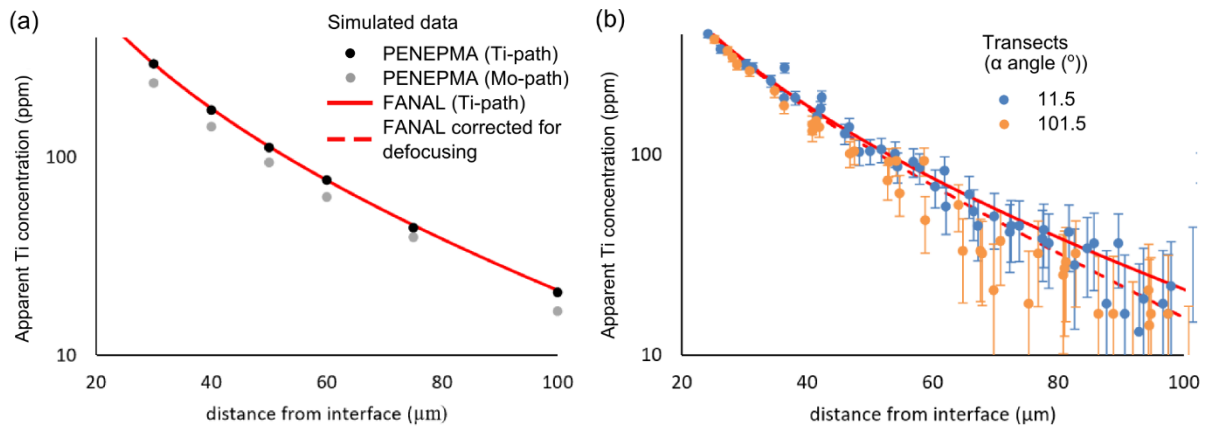
454
455
456
457
458
459

Figure 6 Simulated secondary fluorescence contributions (3a) when the transect is parallel to the focal line of the detector, with x-rays passing along material interface to the detector (3b) as a function of detector azimuthal aperture. Simulations were made for a point along the transect in Al, at a distance of 100 μm from the interface.

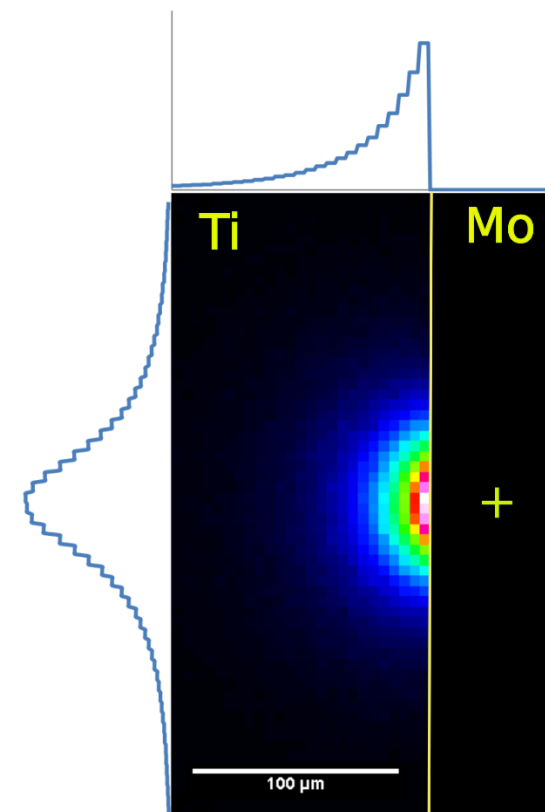


460
461
462
463
464
465
466
467

Figure 7. Comparison of the measurements to the simulated data for different detector configurations, including a realistic simulation where the detector is aligned along the interface with a 10° azimuthal aperture. Using a realistic detector width minimises the mismatch between simulation (red line) and the measured data (blue dots). (b) Schematic showing the geometries of the simulated detectors, and (c) schematic showing the geometry of the sample and instrument detector, where the geometry is overlain on a map of spectrometer defocusing.



468
 469 Figure 8. (a) Comparison of measured, calculated (FANAL) and simulated (PENEPMA) Ti k-ratios versus
 470 beam distance to boundary for a transect in-focus in a Ti-Mo couple. (b) Comparison of measured,
 471 calculated (FANAL) and calculated -and corrected for defocusing effects- (FANAL corrected) Ti k-ratios
 472 for a transect out-of-focus in a Ti-Mo couple. Error bars represent 3 standard deviations of the k-ratio
 473 mean measurements
 474



475
 476 Figure 9. Simulated distribution of secondary fluorescent Ti $K\alpha$ x-rays calculated using PENEPMA, i.e. the
 477 source of secondary fluorescent Ti $K\chi$ x-rays for an analysis made in Mo at 25 μm away from the Mo/Ti
 478 interface. Displayed above and to the left are integrated intensity histograms. Of note is that the x-rays
 479 do not originate from a single point on the interface, but are distributed both along the interface and into
 480 the Ti.